Facile synthesis of phase pure $ZnAl_2O_4$ nanoparticles for effective photocatalytic degradation of organic dyes

Archana Chaudhary[a], Akbar Mohammad[a], Shaikh M. Mobin[a,b,c,*]

[a] Discipline of Chemistry, Indian Institute of Technology Indore, Simrol, Khandwa Road, Indore 453552, India
[b] Center for Biosciences and Bio-Medical Engineering, Indian Institute of Technology Indore, Simrol, Khandwa Road, Indore 453552, India
[c] Discipline of Metallurgy Engineering and Materials Science, Indian Institute of Technology Indore, Simrol, Khandwa Road, Indore 453552, India

ARTICLE INFO

ABSTRACT

The present work focuses on the surfactant mediated synthesis of $ZnAl_2O_4$ nanoparticles ($1-3$) using sol–gel method. **1** has been synthesized without any surfactant and during the synthesis of **2** and **3** cationic (cetyltrimethylammonium bromide) and anionic (sodium lauryl sulfate) surfactant, respectively, have been added. **1–3** have been characterized by P-XRD, FT-IR, SEM, SAED, TEM and BET techniques which suggest that surfactant reduces the particle size of $ZnAl_2O_4$ nanoparticles to half (12 nm in **1**, 6 nm in **2** and **3**). Zeta (ζ) potential measurements have been performed to determine the surface charges of all the samples. Moreover, the photocatalytic activities of these $ZnAl_2O_4$ nanoparticles have also been investigated. **2** exhibits better adsorption (28–41%) and degradation (97–99%) efficiency for anionic dyes due to high surface area (129.62 $m^2 g^{-1}$) and positively charged surface (ζ potential 30.06 mV). Radical trapping experiments suggest $O^{2 \cdot -}$ and $OH^{\cdot}$ to be the major reactive species for the degradation of dyes.

1. Introduction

$ZnAl_2O_4$ spinel belongs to $Fd\overline{3}m$ space group and has a close-packed face-centered cubic structure [1]. In $ZnAl_2O_4$, the valence band is formed by the hybridization of 2p orbitals of O^{2-} and 3d orbitals of Zn^{2+} while the conduction band is made up of 2p and s orbitals of Al^{3+} atom [2,3]. It is transparent for light of the wavelengths > 320 nm, thus, it finds applications in ultraviolet (UV) photoelectronic devices [1]. If the surface area of $ZnAl_2O_4$ spinel is high, it is a useful catalyst and catalyst support as well as photocatalyst for the degradation of dyes [4]. The surface charge of the photocatalyst also plays important role in dye adsorption and degradation process, anionic dyes adsorb well on the surface of a material with the positive value of zeta potential or *vice versa*, due to the attraction of opposite charge particles [5].

It is essential to select an appropriate semiconductor material for degradation of dyes with good efficiency and stability [6]. Among various materials mixed metal oxides containing *d* or *f* orbitals are of special interest as they are assumed to have the extended valance and conduction bands [7]. Due to the extended valance band (VB) and conduction band (CB) the life time of photogenerated carriers increase which further facilitates the redox reaction on the surface of semiconductor material. These photogenerated carriers react faster with corresponding reactive species suppressing the electron-hole recombination and enhancing photocatalytic activity of mixed metal oxide [8].

Heterometallic oxides find applications in fields like- photocatalysts [9–11] and biosensors [12–14]. However, synthesis of these heterometallic systems like $ZnAl_2O_4$ *via* sol-gel route is a bit difficult due to the different rate of hydrolysis and condensation of both the source materials [15]. Use of surfactants as structure directing agents in the sol-gel process is very common as surfactants have natural ability to control the crystal growth of nanomaterials and help in achieving desired morphologies with smaller particle size [16]. Molecules of the surfactants get adsorb on the different crystal planes of the nucleating centres and influence the nucleation process, affecting overall growth and morphology of the nanomaterials [16].

Recently, $ZnAl_2O_4$ nanostructures showing different morphologies have been synthesized through various synthetic routes using different precursors [4,17–23]. Belyaev et al. reported the synthesis of $ZnAl_2O_4$ powder using zinc nitrate solution and boehmite sol precursors via sol-gel method at 750 °C for 3 h [17]. Han et al. synthesized $ZnAl_2O_4$ nanowire arrays *via* an interesting Melt-Injection-Decomposition (MID) method where anodic aluminium oxide (AAO) membrane react with zinc nitrate at 350 °C for 5 h yielding $ZnAl_2O_4$ nanowire arrays [18]. Guo et al. synthesized well-defined hierarchical pore structures of $ZnAl_2O_4$ *via* sol-gel route using zinc chloride and aluminium chloride at

600 °C [19]. Sommer et al. reported nanostructured $ZnAl_2O_4$ by direct spark plasma sintering route using ZnO and α-Al_2O_3 or γ-Al_2O_3 powders in 5 min but they were able to get phase pure $ZnAl_2O_4$ at 1000 °C [20]. Peillon synthesized $ZnAl_2O_4$ spinel using microwave with ZnO and α-Al_2O_3 starting materials at 1350 °C [21]. Foletto et al. synthesized $ZnAl_2O_4$ spinel from zinc nitrate and aluminium nitrate precursors at 700 °C *via* co-precipitation using ammonia solution as a precipitation agent [4].

All the synthetic approaches discussed above either require long reaction time or high temperature or expensive equipment. On contrary, our surfactant mediated synthesis of $ZnAl_2O_4$ nanoparticles using sol–gel method requires shorter reaction time and lower temperature for the growth of crystalline nanoparticles. Herein, we report *"Facile synthesis of phase pure $ZnAl_2O_4$ nanoparticles for effective photocatalytic degradation of organic dyes."*

2. Experimental details

Aluminium isopropoxide {$Al(OPr^i)_3$} and anhydrous zinc acetate {$Zn(OAc)_2$} were used as aluminum and zinc sources, respectively. Al $(OPr^i)_3$ was synthesized by reported method [24]. All the other chemicals and dyes were purchased from Sigma-Aldrich, India. Toluene was dried by the conventional method and further distilled before using [25].

2.1. Synthesis of source material

In a typical procedure, a solution of $Al(OPr^i)_3$ (2.5 g, 12.53 mmol in ~15 ml of toluene) was added to a solution of $Zn(OAc)_2$ (1.16 g, 6.32 mmol in ~15 ml. of toluene) and whole content was refluxed for 3 h. The resulting mixture was concentrated in vaccuo yielding a white solid which was used as the source material for synthesizing $ZnAl_2O_4$.

IR (KBr, cm^{-1}): ν 580 (m), 630 (m), 940 (s), 1056 (s), 1150 (w), 1340 (m), 1455 (m), 1504 (vs), 1555 (s).

Synthesis and characterization of this sort of precursors [$Zn_2Al_2(OPr^i)_6(acac)_4$] [26], [$Zn\{Al(OPr^i)_4\}_2$] [27], [$ZnAl_2(OPri)_{8-n}ONC(CH_3)_2\}_n$] [28], [$ZnAl_2OPr^i)_4(acac)_3(OAc)$] [29] have also been reported in the literature.

2.2. Synthesis of ZnAl2O4 nanoparticles

For the synthesis of $ZnAl_2O_4$, 1.55 g of the precursor was dissolved in 20 ml of isopropanol. 0.2 ml of distilled water was added in this clear solution and stirred for 15 min. Sol formation occurred instantly. Some more amount of water was added to ensure complete hydrolysis, in the time duration of 2 h. This slurry (gel) was separated by centrifugation and washed with water and acetone in order to remove impurities. This sample was kept overnight at room temperature and further sintered at 500 °C for 2 h to generate crystallinity. It was characterized as pure $ZnAl_2O_4$ and coded as **1**.

To examine the role of surfactant on particle size and morphology; 0.1 M solution of cationic surfactant cetyltrimethylammonium bromide, CTAB (for **2**) or anionic surfactant sodium lauryl sulfate, SLS (for **3**) was added during hydrolysis process.

2.3. Photocatalytic experiments

The photocatalytic activity of $ZnAl_2O_4$ was evaluated by the degradation of Eosin B (EB), Congo Red (CR), Methyl Orange (MO), New Methylene Blue (NMB) and Chicago Sky Blue (CSB) dyes using 500 W (λ = 365–366 nm) mercury lamp as light source. For photocatalytic degradation, in 50 ml aqueous solution of Eosin B (15 mg/L), 50 mg of $ZnAl_2O_4$ was added at neutral pH and the suspension was stirred magnetically in the dark for 30 min to attain an adsorption/desorption equilibrium, the whole content was exposed to the mercury lamp at room temperature. Samples were collected at 10 min intervals,

centrifuged and transferred to a quartz cuvette for measuring absorbance by UV–Vis spectroscopy. Finally, the experiments of the photocatalytic degradation of chicago sky blue, congo red, methyl orange and new methylene blue dyes were also performed under the same conditions.

2.4. Determination of reactive species

To identify the major reactive species generated during the photocatalytic degradation, Triethanol amine (TEA) for h^+, *tert*-butyl alcohol (TBA) for $OH^{\cdot}$, and *p*-benzoquinone (BQ) for $O_2^{\cdot-}$ was added into the EB solution as scavengers [30]. The trapping experiments were performed in a similar manner as other dye degradation experiments as aforementioned, except the addition of scavengers before switching on the lamp. The concentration of TEA, TBA, and BQ was taken 0.01, 0.01 and 0.001 mol/L, respectively.

2.5. Characterization

Fourier-transform infrared spectroscopy (FT-IR) spectra were measured with a Bio-Rad FTS 3000MX instrument on KBr pellets in the range of 4000–400 cm^{-1}. Powder X-ray diffraction (P-XRD) were performed on a Rigaku smart lab X-ray diffractometer using monochromated Cu Kα radiation (λ = 0.154 nm). Zeta potentials were measured on a particle size and zeta (ζ) potential analyzer (Micromeritics NanoPlus 3 instrument) using DI water as a solvent. Scanning electron microscopy (SEM) images and Energy dispersive X-ray (EDX) analyses were performed on an EDX coupled Supra55 Zeiss instrument. Transmission electron microscopy (TEM) images were recorded on FEI Tecnai G2 12 Twin TEM instrument. Brunauer-Emmett-Teller (BET) analyses were performed on Belsorp Mini II equipment and the samples were degassed at 300 °C for 2 h at a vacuum pressure of 10–2 kPa. UV spectra for dye degradation were recorded on a Cary-100 Bio UV–Vis spectrophotometer and solid state UV spectra of $ZnAl_2O_4$ spinel were recorded on a PerkinElemer UV–Vis spectrophotometer.

3. Results and discussion

$ZnAl_2O_4$ nanoparticles were synthesized *via* sol-gel route as depicted in Scheme 1 and were characterized by P-XRD, FT-IR, SEM, TEM, EDX and BET techniques.

3.1. Structural and Morphological characterization

The P-XRD patterns of **1**–**3** confirmed that the synthesized $ZnAl_2O_4$ samples crystallized in face centered cubic phase and were phase pure (2θ = 31.2°, 36.8°, 44.8°, 49.1°, 55.6°, 59.3°, 65.2°, 74.2°, 77.3°, 90.9°, 94.1°, 11.2°; ICDD data #05-0669; Fig. 1) [4]. The average particle size of $ZnAl_2O_4$ was calculated using Scherrer's formula [31] and found to be 12 nm in **1** (without using surfactant) and decreased to 50% (*i.e.,* 6 nm) on using the surfactant in **2** and **3**. It is necessary to mention here
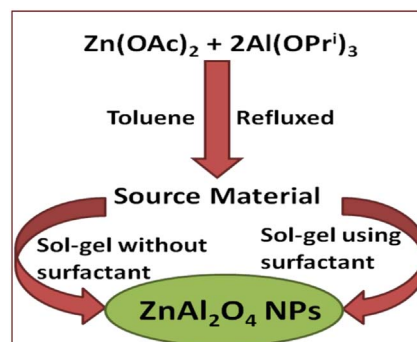
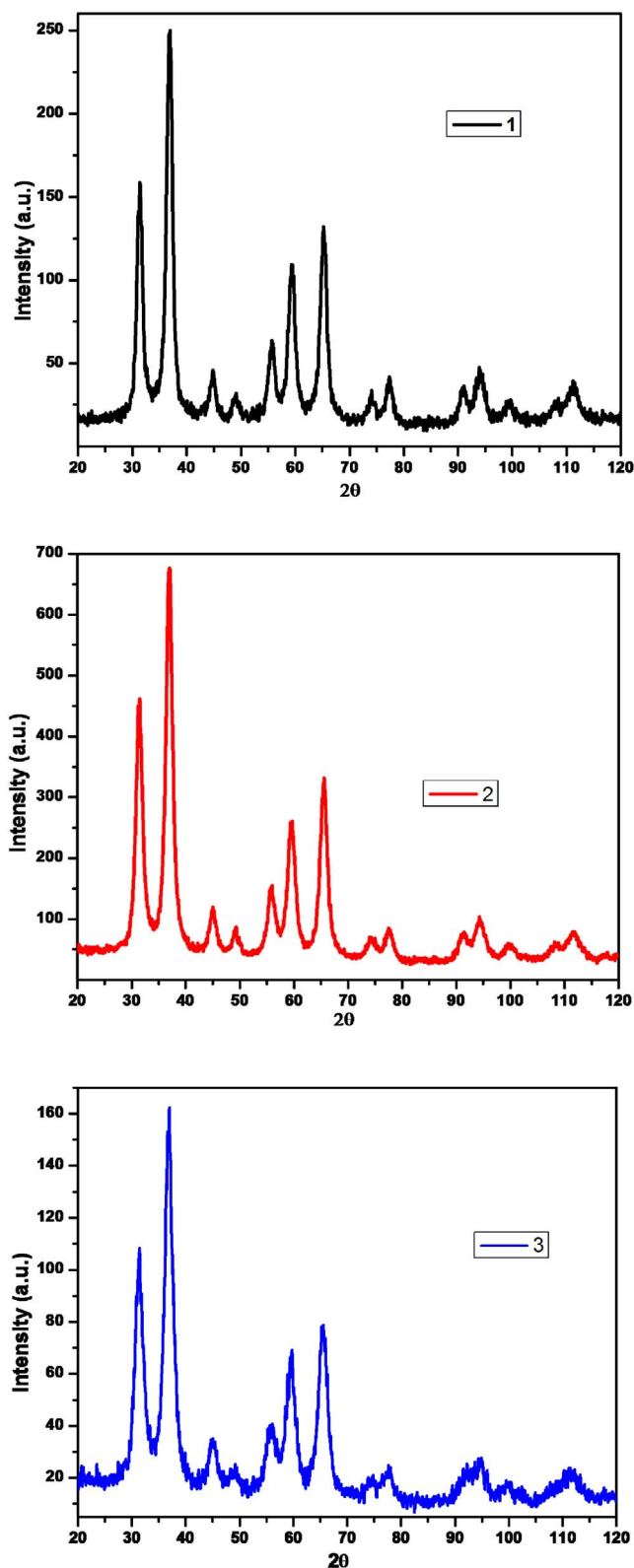**Scheme 1.** Schematic representation of the synthesis of $ZnAl_2O_4$.

Fig. 1. XRD Patterns of **1**–**3**.

that when Al(OPr^i)$_3$ and Zn(OAc)$_2$ were dissolved directly in methanol to synthesize ZnAl$_2$O$_4$, three unidentified diffraction peak (2θ = 23.7°, 26.4° and 27.9°), with very low intensity were observed in the XRD patterns (Fig. S1).

Formation of ZnAl$_2$O$_4$ was also confirmed by FTIR spectra of sample **1**–**3** (Fig. S2). In the IR spectra, the bands around 660 cm^{-1} and

550 cm^{-1} were attributed to the AlO$_6$ groups, building up the ZnAl$_2$O$_4$ spinel. The absence of peaks in the region 700–850 cm^{-1} further confirmed spinel structure of ZnAl$_2$O$_4$. However, all the samples exhibited common broad bands near 3450 and 1650 cm^{-1} due to the –OH stretching of H$_2$O molecules. The broadening of the band was due to hydrogen bond formation. The band observed near 1650 cm^{-1} was attributed to the bending vibration of interlayer water molecules, which was probably due to the absorption of water during sample preparation with KBr or rapid adsorption of water due to the very high surface area of the samples [32].

Surface morphologies of these samples were examined by SEM images. In all the samples high degree of agglomeration was observed (Fig. S3). Although surfactants act as a clear structure directing agents [16], controlling agglomeration, size and shape of the nanomaterials but in our case both the surfactants controlled the particle size of the nanomaterials and not the shape. EDS spectra (inset of Fig. S3) showed the presence of Zn, Al and O elements in the prepared samples. TEM images also corroborated the results of P-XRD and further confirmed the presence of tiny particles in all the three samples (Fig. 2).

The nitrogen adsorption–desorption isotherm and pore size distribution curve for samples **1**–**3** are depicted in Fig. 3(a–f) and values of the specific surface area, pore volume and pore radius are given in Table 1. Analysis of porosity was carried out by applying BJH method to the adsorption branch of each isotherm for analyzing porosity of the samples [4]. The isotherms of **1**–**3** were of type IV according to the IUPAC classification [33] showing a hysteresis loop at a high relative pressure, which advocated that samples **1**–**3** were mesoporous in nature. Higher surface area of **2** as compared to **1** and **3** may be due to use of surfactant CTAB during the synthesis of **2** [34].

The light absorbance of samples **1**–**3** was evaluated by the UV–Vis spectroscopy and the results are shown in Fig. 4a. Band gap of **1**–**3** were determined by Tauc relation [35] and were calculated to be 3.49 eV, 3.81 eV and 4.24 eV for **1**, **2** and **3**, respectively (Fig. 4b). Generally, when the particle size decreases there is an increase in the band gap energy [36] but decrease of band gap in **1** than reported literature (*i.e.,* 3.8 eV) may be due the presence of more defect levels in the conduction band (CB) and the valence band (VB) of prepared sample [37,38].

To study the surface charge in the solution, zeta potentials of **1**–**3** were also measured in water. The values of ζ potential were found to be 27.58 mV (**1**), 30.06 mV (**2**) and 9.87 mV (**3**) (Fig. 5). It is worthy to mention here that as the surface of the ZnAl$_2$O$_4$ spinel was positively charged in the **1** (which was synthesized without any surfactant); the charge of the surface did not vary much on adding a cationic surfactant (*i.e.,* CTAB) in **2** whereas on adding an anionic surfactant (*i.e.,* SLS) in **3**, a considerable decrease in the zeta potential was observed [39].

3.2. Adsorption and catalytic degradation

Photocatalytic activities of ZnAl$_2$O$_4$ spinel were studied using various organic dyes. Due to larger surface area, **2** was explored further for photocatalytic studies. Eosin B was chosen as the model dye because it showed maximum degradation in minimum time. Eosin B has a characteristic peak at 517 nm, which was used to monitor the photocatalytic degradation [40]. For the performance of the photocatalysis of ZnAl$_2$O$_4$, 50 mg of catalyst and 50 ml aqueous solution of Eosin B were utilized. The degradation of dye could clearly be observed by looking at the aqueous solution of dye by naked eyes. Eosin B did not degrade under the influence of light irradiation without using the catalyst (Fig. S4) or using ZnAl$_2$O$_4$ catalyst but switching off the lamp (Fig. S5). In the sunlight, the degradation occurred very slowly and degraded only 56.5% of the dye (Fig. S6). Using ZnAl$_2$O$_4$ photocatalyst at room temperature with switching on the mercury lamp, 98.9% degradation of Eosin B was observed within 40 min only (Fig. 6a). The degradation for Congo Red (CR), Chicago Sky Blue (CSB), Methyl Orange (MO) and Mew Methylene Blue (NMB) dyes was observed to be 98.3%, 97.2%, 96.9%, and 90.2%, respectively {Fig. 6(b–e) and Table 2}.
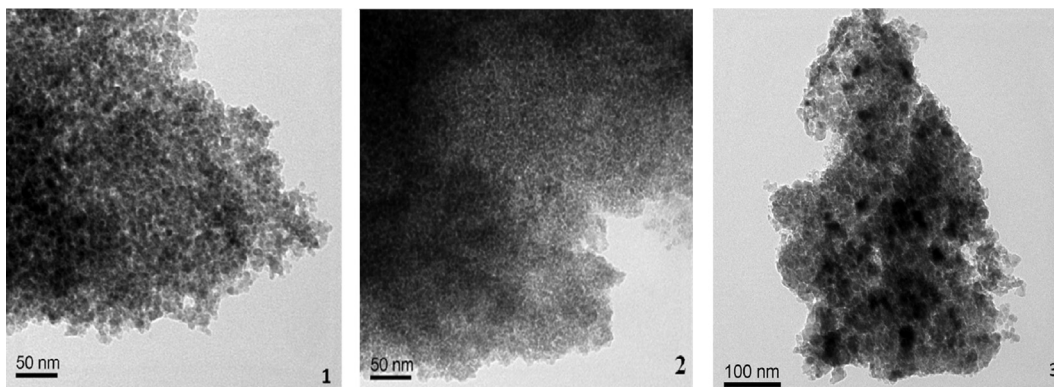
Fig. 2. TEM images of **1–3**.

The surface charge of the catalyst **2** also played a significant role in the adsorption and degradation process [41,42]. All the anionic dyes showed more than 96% degradation on the surface of **2** whereas the cationic dye NMB showed only 90.2% degradation. Similarly, all the anionic dyes adsorbed well on the surface of catalyst (Table 2) whereas only 9.2% of NMB adsorbed on the surface **2**, due to the repulsion among similarly charged species. To further investigate the role of surface charge, we used sample **3** (ζ potential 9.87 mV) for adsorption and degradation of the cationic dye, NMB. On the surface of **3**, cationic dyes showed better adsorption (14.4%) and degradation 93.7% than **2** (Fig. 6f and S7). The particle sizes of both the samples were approx 6 nm, and specific surface area of **3** is less than **2**, but better adsorption and degradation of NMB on the surface of **3** further amplified the role of surface charges of the catalyst.

The difference in photocatalytic activities of catalyst towards all the dyes used (MO, CR, CSB, EB and NMB), may be due to the difference in kinetic behavior of these dyes for photocatalytic degradation reaction.

Table 1
Textural properties of ZnAl$_2$O$_4$ samples.

Sample	Specific surface area ($m^2 g^{-1}$)	Average pore size (nm)	Total pore volumes ($cm^3 g^{-1}$)
1	78.59	2.38	0.09
2	129.62	2.38	0.16
3	82.41	3.53	0.15

To further investigate the photocatalytic activities of these samples, the photocatalytic degradation kinetics was analyzed using pseudo-first-order kinetics:

$$\ln (C_0/C) = kt$$

where k = pseudo-first-order rate kinetic constant (min^{-1}); t = irradiation time (min); C = concentration and C_0 = initial concentration ($mg\ L^{-1}$) of the reactant.
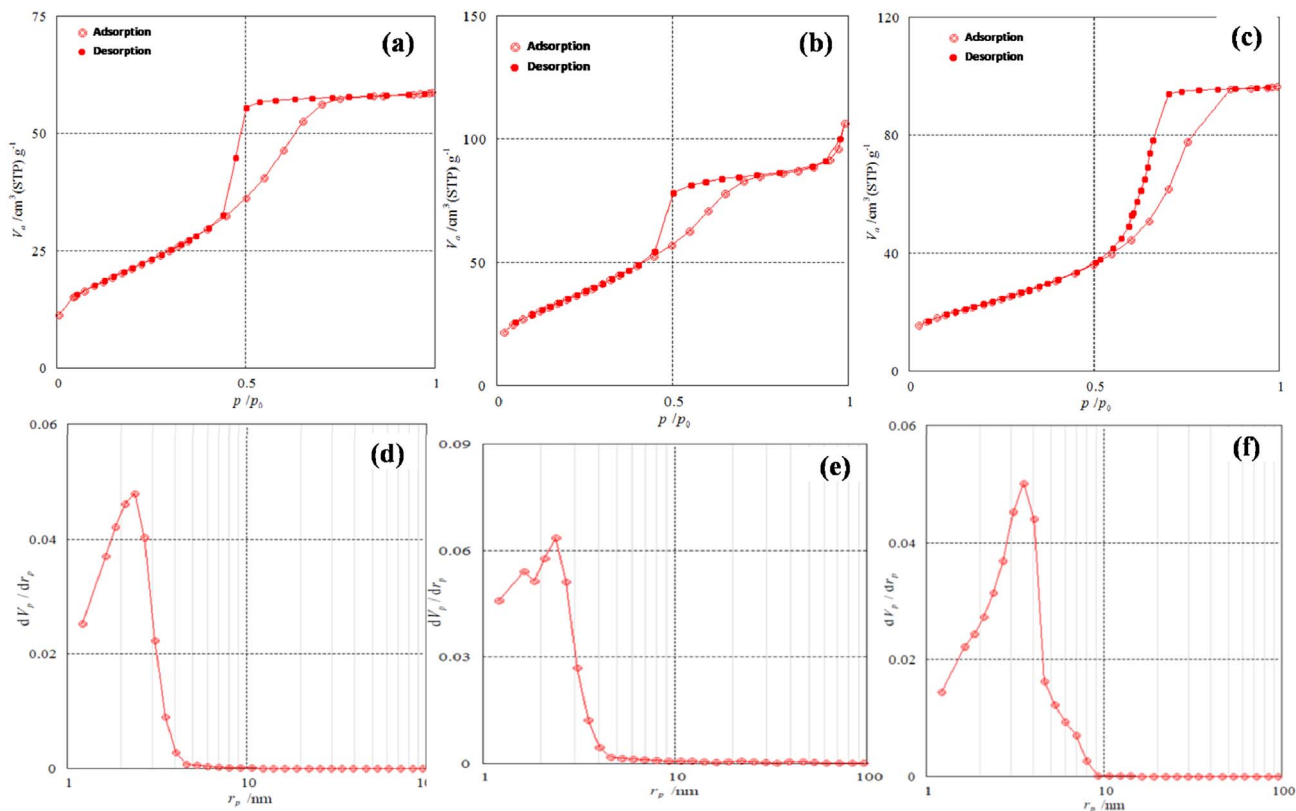

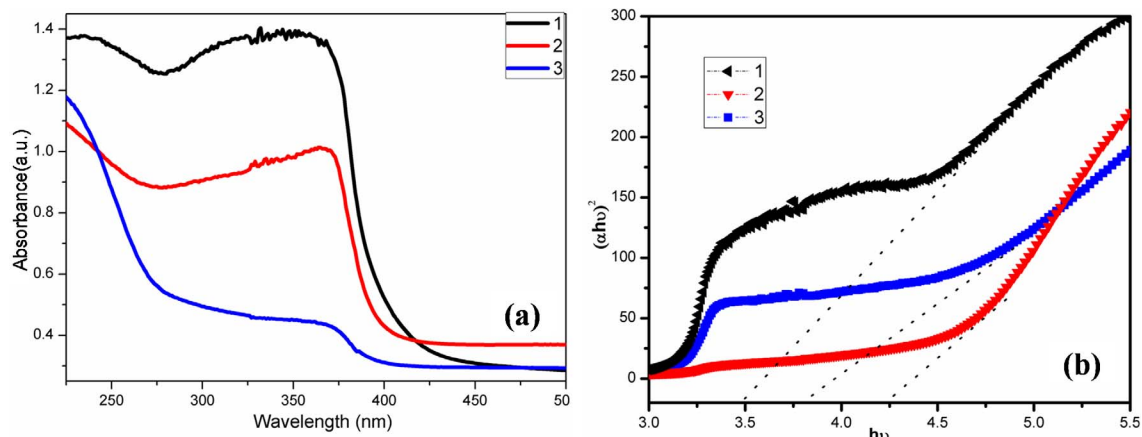**Fig. 3.** (a-c) Adsorption/desorption isotherms of **1–3** and (d-e) BJH plots of **1–3**.

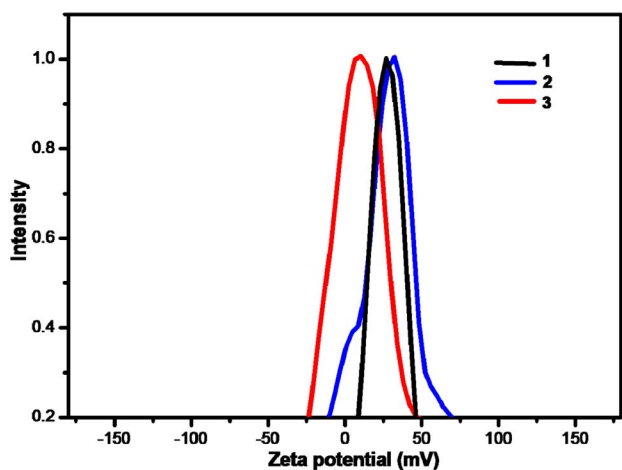Fig. 4. Absorption spectra and Band gap diagrams of **1–3**.

Fig. 5. Zeta Potential measurements of **1–3**.

Table 2
Dye adsorption and degradation efficiency of **2**.

Dye	Adsorption	Degradation	Rate constant (min^{-1})
Eosin B (EB)	30.1%	98.9%	$7.10 * 10^{-2}$
Congo Red (CR)	27.8%	98.3%	$3.25 * 10^{-2}$
Chicago Sky Blue (CSB)	41.4%	97.2%	$3.38 * 10^{-2}$
Methyl Orange (MO)	40.8%	96.9%	$3.16 * 10^{-2}$
New Methylene Blue (NMB)	9.2%	90.2%	$2.36 * 10^{-2}$

The variations in C/C_0 as a function of irradiation time and $\ln C/C_0$ as a function of irradiation time are given in Fig. 7(a and b) and the value of rate constants are given in Table 2.

Results of the photocatalytic degradation of Eosin dye using $ZnAl_2O_4$ spinel were compared with other reported photocatalysts (Table 3) which suggested that $ZnAl_2O_4$ is a better photocatalyst with respect to the time and degradation efficiency.
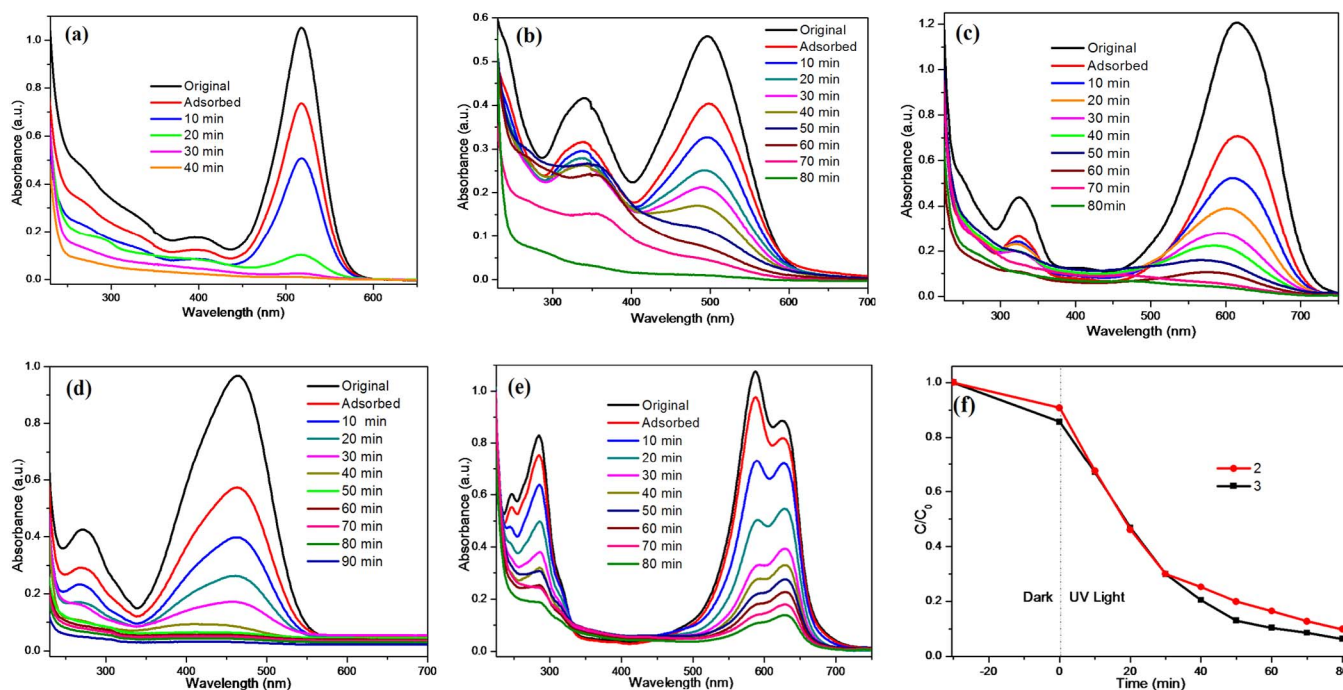

Fig. 6. Absorption spectra of (a) Eosin B (b) Congo Red (c) Chikago Sky Dye (d) Methyl Orange (e) New Methylene Blue solutions showing photocatalytic degradation using $ZnAl_2O_4$ spinel (f) Comparative photo-catalytic degradation of New Methylene Blue (NMB) solution using **2** and **3**. (For interpretation of the references to colour in this figure legend, the reader is referred to the web version of this article.)
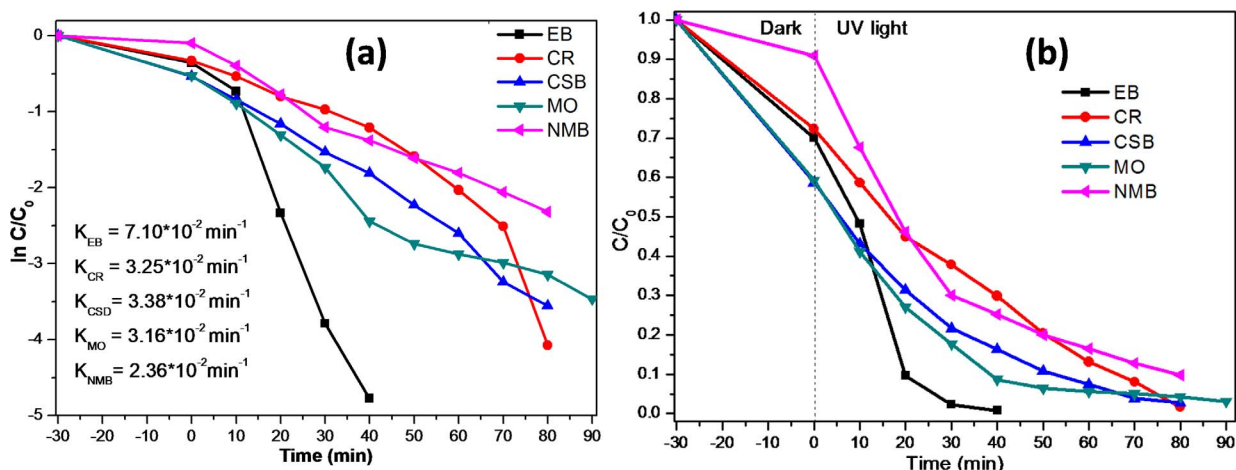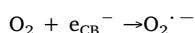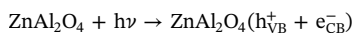
Fig. 7. (a) Kinetic linear simulation curves of $ZnAl_2O_4$ spinel with five different organic dyes (b) Photocatalytic degradation rate of $ZnAl_2O_4$ spinel on five organic dyes.

3.3. Radical tapping experiments

To further investigate the responsible radical for dye degradation radical trapping experiments were performed. In this study, different scavengers, *i. e.* Triethanol amine (TEA) for h^+, *tert*-butyl alcohol (TBA) for $OH^.$, and *p*-benzoquinone (BQ) for $O_2^{.-}$ were used. It is evident from Fig. 8a that all scavengers were capable of decreasing the degradation of EB to some extent. The degradation of EB reduced from 98.9% to 16%, 24.4% and 45.1%, in the presence of BQ, TBA and TEA, respectively. These trapping experiments suggested that $O_2^{.-}$ and $OH^.$ were the key radicals for the degradation of EB, however, h^+ radical was also able to degrade the dye to some extent (Fig. 8b). These results are in accordance with Zhang et al. recent report where they proposed that under UV light $O_2^{.-}$ and $OH^.$ are more reactive species for degradation of dyes [30].

3.4. Plausible mechanism for degradation of dyes

Following plausible mechanism may be proposed for the degradation of dyes using $ZnAl_2O_4$ nanoparticles [49]-

$$ZnAl_2O_4 + h\nu \rightarrow ZnAl_2O_4(h_{VB}^+ + e_{CB}^-)$$

$$h_{VB}^+ + H_2O/OH^- \rightarrow OH^.$$

$$O_2 + e_{CB}^- \rightarrow O_2^{.-}$$

$$Dye + O_2^{.-}/OH^./h^+ \rightarrow Degradation\ product + CO_2 + H_2O$$

As UV light falls on the surface of the catalyst, electrons (e^-) of the

valance band (VB) get excited and move to the conduction band (CB), leaving the holes (h^+) behind in the CB. These holes present in the VB either oxidize the dye molecules directly or indirectly by reacting with water or OH^- (adsorbed on the surface of the catalyst), producing $OH^.$. The conduction band electrons reduce the oxygen present on the surface of $ZnAl_2O_4$ to $O_2^{.-}$ which further reacts with the active dye molecules, converting them into other degradation products (Fig. 8b). The possible degradation products of eosin dye by LC–MS were also investigated [51]. Identified intermediate products are shown in Scheme 2 and Fig. S8.

3.5. Reusability test

For practical applications of a photocatalyst, the reusability is as important as its efficiency. To evaluate the reusability of $ZnAl_2O_4$ nanoparticles, four consecutive photocatalytic experimental runs were performed, adding recycled $ZnAl_2O_4$ photocatalyst to fresh EB solutions. The activity of $ZnAl_2O_4$ particles for the degradation of EB was observed upto four cycles (Fig. 9a). To observe the changes in the crystal structure of the used $ZnAl_2O_4$, P-XRD patterns were recorded which illustrated no change in the crystal structure of $ZnAl_2O_4$ after photocatalytic activity (Fig. 9b), and insignificant change in the surface morphology (Fig. S9), signifying the use of synthesized $ZnAl_2O_4$ spinel as a reusable photocatalyst for the oxidation of pollutant molecules.

4. Conclusions

In summary, *Phase pure* $ZnAl_2O_4$ spinels have been synthesized by

Table 3
Comparison of performance of $ZnAl_2O_4$ against Eosin dye with the recently reported photocatalysts.

| Materials	Degradation efficiency	Time	Initial conc. of dye	Catalyst loading	Source	References
ZnO/ZnS heterostructures	96.1%	70 min	10 mg/L	50 mg	Xenon lamp	[40]
Fe_2O_3 doped Co	78%	180 min	$5 * 10^{-5}$ M	300 mg	Microwave	[43]
Fe_2O_3 doped Co	83%	180 min	$5 * 10^{-5}$ M	300 mg	Ultrasound	[43]
Fe_2O_3 doped Co	82%	180 min	$5 * 10^{-5}$ M	300 mg	Solar irradiation	[43]
Fe_2O_3 doped Co	87%	180 min	$5 * 10^{-5}$ M	300 mg	Ultrasound + Solar irradiation	[43]
CdS dendritic	95%	100 min	10 mg/L	50 mg	Xenon lamp	[44]
Graphene-TiO_2	47%	120 min	$0.1 * 10^{-4}$ M	1 cm^2 (electrode area)	Photoelectrochemical	[45]
SnS QDs	91.7%	60 min	20 mg/L	25 mg	Solar irradiation	[46]
Cu_2SnS_3/r-GO (3%) composite	92%	140 min	7.5 mg/L	100 mg	Tungsten-Halogen lamp	[47]
MnO_2	96%	35 min	40 mg/L	100 mg	Mercury lamp	[48]
ZnO_2/SnO_2 hetero-nanofibers	98.9%	70 min	10 mg/L	50 mg	Mercury lamp	[49]
ZnO nanoflower	95.9%	80 min	15 mg/L	20 mg	Mercury lamp	[50]
$ZnAl_2O_4$	98.9%	40 min	15 mg/L	50 mg	Mercury lamp	This work
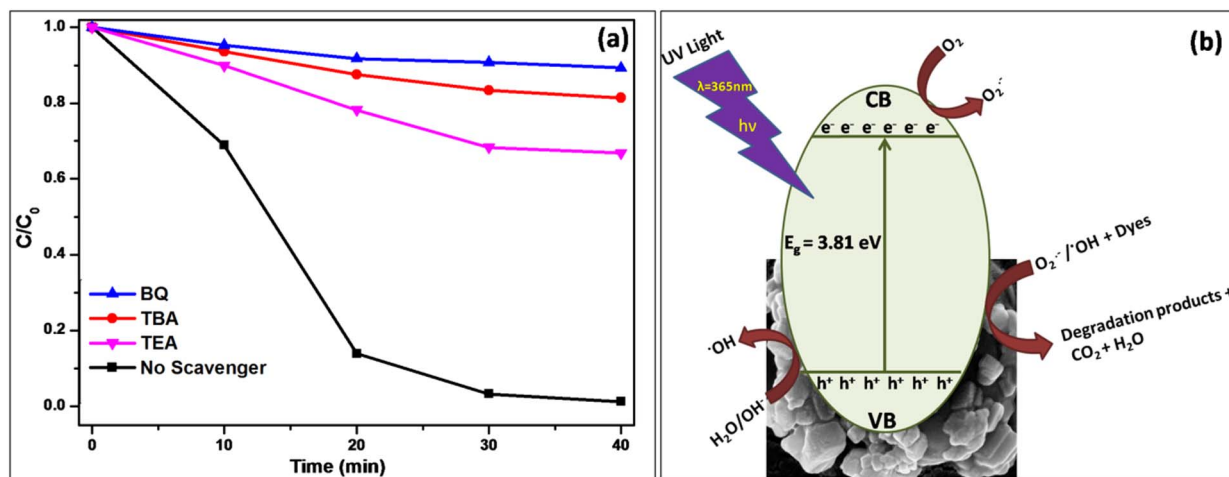
Fig. 8. (a) Effect of different scavengers on the degradation of EB in the presence of the $ZnAl_2O_4$ Photocatalyst under UV light irradiation (b) Plausible photocatalytic reaction pathway of Dyes over $ZnAl_2O_4$ Photocatalyst under UV illumination.

surfactant mediated sol-gel method and characterized using various sophisticated techniques. The effect of cationic (CTAB) and anionic (SLS) surfactants on the size and morphology of synthesized nanoparticles have also been studied. Both the surfactants do not affect the morphology of the samples, however, decrease the particle size of $ZnAl_2O_4$ to 6 nm (**2** and **3**) from 12 nm (**1**). Photocatalytic activities of $ZnAl_2O_4$ nanoparticles have also been evaluated. Small particle size and high surface area make the synthesized $ZnAl_2O_4$ spinel a suitable candidate for adsorption and degradation of organic dyes. Further, good stability and reusability advocate its practical application in dye industry.

Acknowledgements
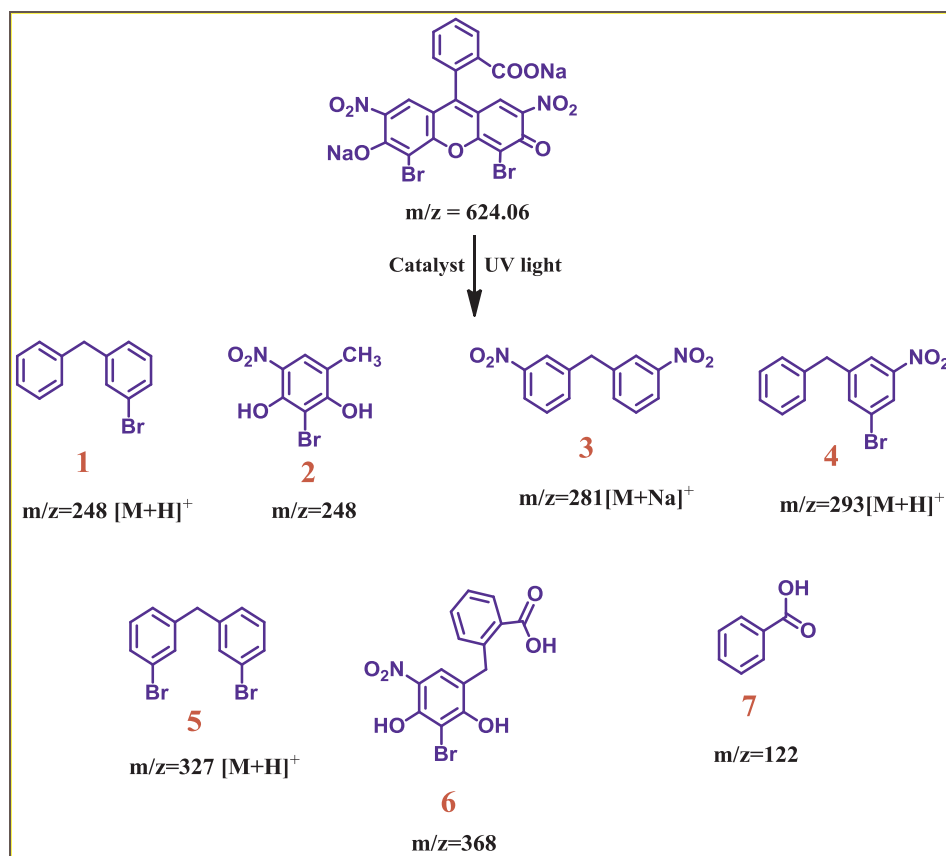
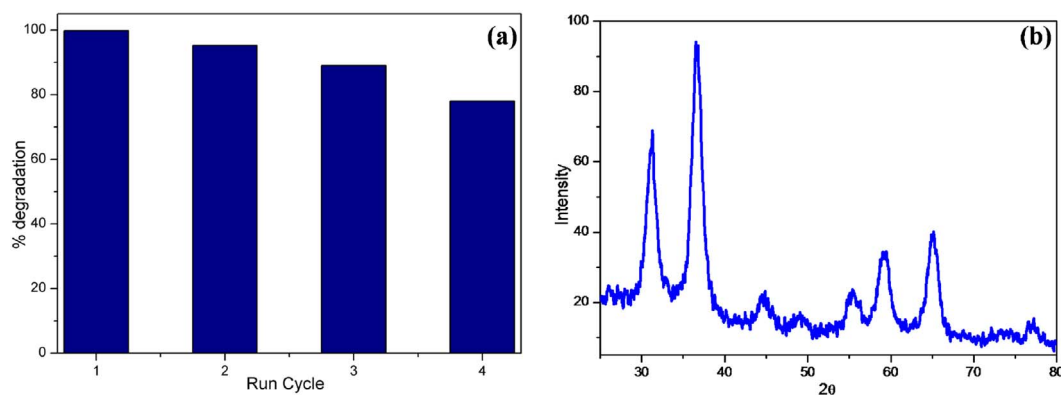**Scheme 2.** Possible products obtained by photocatalytic degradation of Eosin B.

Fig. 9. (a) Cycling tests of photocatalytic activity of the ZnAl$_2$O$_4$ spinel for the degradation of Eosin B (b) PXRD patterns of ZnAl$_2$O$_4$ (sample 2) after using as photocatalyst.

Appendix A. Supplementary data

Supplementary data associated with this article can be found, in the online version, at http://dx.doi.org/10.1016/j.mseb.2017.10.009.

References

[1] R.J. Wiglusz, T. Grzyb, A. Bednarkiewicz, S. Lis, W. Strek, Investigation of structure, morphology, and luminescence properties in blue-red emitter, europium-activated ZnAl$_2$O$_4$ nanospinels, Eur. J. Inorg. Chem. 3418–3426 (2012).
[2] S.K. Sampath, D.G. Kanhere, R. Pandey, Electronic structure of spinel oxides: zinc aluminate and zinc gallate, J. Phys. Condens. Matter 11 (1999) 3635–3644.
[3] F. Zerarga, A. Bouhemadou, R. Khenata, S. Bin-Omran, Structural, electronic and optical properties of spinel oxides ZnAl$_2$O$_4$, ZnGa$_2$O$_4$ and ZnIn$_2$O$_4$, Solid State Sci. 13 (2011) 1638–1648.
[4] E.L. Foletto, S. Battiston, J.M. Simões, M.M. Bassaco, E.I. Müller, Synthesis of ZnAl$_2$O$_4$ nanoparticles by different routes and the effect of its pore size on the photocatalytic process, Micropor. Mesopor. Mater. 163 (2012) 29–33.
[5] M. Miyauchi, A. Ikezawa, H. Tobimatsu, H. Iriea, K. Hashimoto, Zeta potential and photocatalytic activity of nitrogen doped TiO$_2$ thin films, Phys. Chem. Chem. Phys. 6 (2004) 865–870.
[6] M. Shekofteh-Gohari, A. Habibi-Yangjeh, Fe$_3$O$_4$/ZnO/CoWO$_4$ nanocomposites: novel magnetically separable visible-light-driven photocatalysts with enhanced activity in degradation of different dye pollutants, Ceram. Int. 43 (2017) 3063–3071.
[7] H.W. Eng, P.W. Barnes, B.M. Auer, P.M. Woodward, Investigations of the electronic structure of d^0 transition metal oxides belonging to the perovskite family, J. Solid State Chem. 175 (2003) 94–109.
[8] R. Ullah, H. Sun, H.M. Ang, M.O. Tadé, S. Wang, Visible light photocatalytic degradation of organics on nanoparticles of bi-metallic oxides, Sep. Purif. Technol. 89 (2012) 98–106.
[9] M. Mumjitha, V. Raj, Electrochemical synthesis, structural features and photoelectrocatalytic activity of TiO$_2$-SiO$_2$ ceramic coatings on dye degradation, Mater. Sci. Eng. B 198 (2015) 62–73.
[10] B. Paul, B. Bhuyan, D.D. Purkayastha, S.S. Dhar, S. Behera, Facile synthesis of spinel CuCr$_2$O$_4$ nanoparticles and studies of their photocatalytic activity in degradation of some selected organic dyes, J. Alloys Compounds 648 (2015) 629–635.
[11] R.M. Kong, X. Zhao, Y. Zheng, F. Qu, Facile synthesis of ZnO/CdS@ZIF-8 core-shell nanocomposites and their applications in photocatalytic degradation of organic dyes, RSC Adv. 7 (2017) 31365–31371.
[12] J. Shu, Z. Qiu, Z. Lin, G. Cai, H. Yang, D. Tang, Semiautomated support photoelectrochemical immunosensing platform for portable and high-throughput immunoassay based on Au nanocrystal decorated specific crystal facets BiVO$_4$ photoanode, Anal. Chem. 88 (2016) 12539–12546.
[13] S. Lv, K. Zhang, Z. Lin, D. Tang, Novel photoelectrochemical immunosensor for disease-related protein assisted by hemin/G-quadruplex-based DNAzyme on gold nanoparticles to enhance cathodic photocurrent on p-CuBi$_2$O$_4$ semiconductor, Biosens. Bioelectron. 96 (2017) 317–323.
[14] K. Zhang, S. Lv, Z. Lin, D. Tang, CdS: Mn quantum dot-functionalized g-C$_3$N$_4$ nanohybrids as signalgeneration tags for photoelectrochemical immunoassay of prostate specific antigen coupling DNAzyme concatamer with enzymatic biocatalytic precipitation, Biosens. Bioelectron. 95 (2017) 34–40.
[15] R.C. Mehrotra, A. Singh, S. Sogani, Homo- and heterometallic alkoxides of group 1, 2, and 12 metals, Chem. Soc. Rev. 23 (1994) 215–225.
[16] M.S. Bakshi, How surfactants control crystal growth of nanomaterials, Cryst. Growth Des. 16 (2016) 1104–1133.
[17] A.V. Belyaev, I.I. Evdokimov, V.V. Drobotenko, A.A. Sorokin, A new approach to producing transparent ZnAl$_2$O$_4$ ceramics, J. Eur. Ceram. Soc. 37 (2017) 2747–2751.
[18] D. Han, Low-temperature synthesis and photoluminescence properties of oriented ZnAl$_2$O$_4$ nanowire arrays, Superlattices Microstruct. (2017), http://dx.doi.org/10.1016/j.spmi.2017.08.012.
[19] X. Guo, P. Yin, W. Lei, H. Yang, K. Nakanishi, Synthesis and characterization of monolithic ZnAl$_2$O$_4$ spinel with well-defined hierarchical pore structures via a sol-gel route, J. Alloys Compd. (2017), http://dx.doi.org/10.1016/j.jallcom.2017.08.172.
[20] S. Sommer, E.D. Bøjesen, A.B. Blichfeld, B.B. Iversen, Tailoring band gap and thermal diffusivity of nanostructured phase-pure ZnAl$_2$O$_4$ by direct spark plasma sintering synthesis, J. Solid State Chem. (2017), http://dx.doi.org/10.1016/j.jssc.2017.08.023.
[21] N. Peillon, F. Zuo, C. Meunier, S. Saunier, D. Goeuriot, In-situ studies on preparation of ZnAl$_2$O$_4$ spinel using microwave reactive sintering technique, Mater. Lett. 167 (2016) 77–80.
[22] S.-F. Wang, G.-Z. Sun, L.-M. Fang, L. Lei, X. Xiang, X.-T. Zu, A comparative study of ZnAl$_2$O$_4$ nanoparticles synthesized from different aluminum salts for use as fluorescence materials, Sci. Rep. 5 (2015) 12849.
[23] L. Cornu, M. Gaudon, V. Jubera, ZnAl$_2$O$_4$ as a potential sensor: variation of luminescence with thermal history, J. Mater. Chem. C 1 (2013) 5419–5428.
[24] A.R. Sanwaria, M. Nagar, R. Bohra, A. Chaudhary, S.M. Mobin, P. Mathur, B.L. Choudhary, Sol–gel synthesis of highly pure α-Al$_2$O$_3$ nano-rods from a new class of precursors of salicylaldehyde-modified aluminum(III) isopropoxide. Crystal and molecular structure of [Al(OC$_6$H$_4$CHO)$_3$], RSC Adv. 4 (2014) 30081–30089.
[25] A.I. Vogel, Text Book of Quantitative Chemical Analysis, fifth ed., Longmans, London, 1989.
[26] V.G. Kessler, S. Gohil, S. Parola, Interaction of some divalent metal acetylacetonates with Al, Ti, Nb and Ta isopropoxides. Factors influencing the formation and stability of heterometallic alkoxide complexes, Dalton Trans. (2003) 544–550.
[27] S. Mathur, M. Veith, M. Haas, H. Shen, N. Lecerf, V. Huch, S. Hüfner, R. Haberkorn, H.P. Beck, M. Jilavi, Single-source sol-gel synthesis of nanocrystalline ZnAl$_2$O$_4$: structural and optical properties, J. Am. Ceram. Soc. 84 (2001) 1921–1928.
[28] J. Jain, M. Nagar, Synthesis and characterization of some acetoxime-modified hetero-metal alkoxide precursors of zinc(II) and aluminum(III) for sol–gel transformation to nano-sized ZnAl$_2$O$_4$, J. Sol-Gel Sci. Technol. 71 (2014) 447–457.
[29] A.G.A. Seisenbaeva, E.V. Suslova, M. Kritikos, V.G. Kessler, L. Rapenne, M. Andrieux, F. Chassagneux, S. Parola, Purposeful construction versus self-assembly in approaches to single source precursors of spinel materials. Synthesis, structure and stability studies of MIIAl2(acac)3(OiPr)4(OAc), MII = Mn Co, Zn - a new class of heterometallic heteroleptic alkoxide Complexes, J. Mater. Chem. 14 (2004) 3150–3157.
[30] T. Zhang, W. Lei, P. Liu, J.A. Rodriguez, J. Yu, Y. Qi, G. Liu, M. Liu, Organic pollutant photodecomposition by Ag/KNbO$_3$ nanocomposites: a combined experimental and theoretical study, J. Phys. Chem. C 120 (2016) 2777–2786.
[31] B.E. Warren, X-ray Diffraction, Dover publication, New York, 1990, p. 13.
[32] X. Wei, D. Chen, Synthesis and characterization of nanosized zinc aluminate spinel by sol–gel technique, Mater. Lett. 60 (2006) 823–827.
[33] S. Wang, G.Q. Lu, A comprehensive study on carbon dioxide reforming of methane over Ni/γ-Al$_2$O$_3$ catalysts, Ind. Eng. Chem. Res. 38 (1999) 2615–2625.
[34] M. Khalid, M. Mujahid, S. Amin, R.S. Rawat, A. Nusair, G.R. Deen, Effect of surfactant and heat treatment on morphology, surface area and crystallinity in hydroxyapatite nanocrystals, Ceram. Int. 39 (2013) 39–50.
[35] J. Tauc, Amorphous and Liquid Semiconductors, Plenum, New York, 1974.
[36] A. Chaudhary, N. Sharma, V. Dhayal, A. Saxena, M. Nagar, R. Bohra, Synthesis and characterization of some bis (cyclopentadienyl) titanium (IV) complexes with internally functionalized oximes (LH): sol–gel transformations of Cp$_2$TiCl$_2$, Cp$_2$TiClL and Cp$_2$TiL$_2$ to nano-sized anatase titania, Appl. Organomet. Chem. 25 (2011) 198–206.
[37] H. Tajizadegan, O. Torabi, A. Heidary, M.-H. Golabgir, Influence of different alumina precursors on structural properties and morphology of ZnO-Al$_2$O$_3$ nano-composite powder, Int. J. Appl. Ceram. Technol. 1–8 (2015).
[38] H. Nian, S.H. Hahn, K.-K. Koo, J.S. Kim, S. Kim, E.W. Shin, E.J. Kim, Preparation and characterization of sol–gel Li and Al codoped ZnO thin films, Mater. Lett. 64 (2010) 157–160.
[39] W. Jia, S. Ren, B. Hu, Effect of water chemistry on zeta potential of air bubbles, Int. J. Electrochem. Sci. 8 (2013) 5828–5837.
[40] W. Jia, B. Jia, F. Qu, X. Wu, Towards a highly efficient simulated sunlight driven photocatalyst: a case of heterostructured ZnO/ZnS hybrid structure, Dalton Trans. 42 (2013) 14178–14187.

[41] M. Dai, The effect of zeta potential of activated carbon on the adsorption of dyes from aqueous solution: I. The adsorption of cationic dyes: methyl green and methyl violet, J. Colloid Interface Sci. 164 (1994) 223–228.

[42] K. Huang, Y. Lv, W. Zhang, S. Sun, B. Yang, F. Chi, S. Ran, X. Liu, One-step synthesis of Ag_3PO_4/Ag photocatalyst with visible-light photocatalytic activity, Mat. Res. 18 (2015) 939–945.

[43] A. Sharfalddin, E. Alzahrani, M. Alamoudi, Micro, sono, photocatalytic degradation of eosin B using ferric oxide doped with cobalt, ACSJ 13 (2016) 1–13. Article no. ACSJ.23648.

[44] Z. Yu, X. Wu, J. Wang, W. Jia, G. Zhub, F. Qu, Facile template-free synthesis and visible-light driven photocatalytic performances of dendritic CdS hierarchical structures, Dalton Trans. 42 (2013) 4633–4638.

[45] B. Ntsendwana, S. Sampath, B.B. Mambaa, O.A. Arotiba, Photoelectrochemical oxidation of p-nitrophenol on an expanded graphite–TiO_2 electrode, Photochem. Photobiol. Sci. 12 (2013) 1091–1102.

[46] A.P. Chowdhury, B.H. Shambharkar, S.G. Ghugal, S.S. Umare, A.G. Shende, Ethylene glycol mediated synthesis of SnS quantum dots and their application

towards degradation of eosin yellow and brilliant green dyes under solar irradiation, RSC Adv. 6 (2016) 108290–108297.

[47] S. Vadivel, D. Maruthamani, B. Paul, S.S. Dhar, A. Habibi-Yangjeh, S. Balachandran, B. Saravanakumar, A. Selvakumara, K. Selvam, Biomolecule-assisted solvothermal synthesis of Cu_2SnS_3 flowers/RGO nanocomposites and their visible-light-driven photocatalytic activities, RSC Adv. 6 (2016) 74177–74185.

[48] B. Yin, S. Zhang, Y. Jiao, Y. Liu, F. Qu, X. Wu, Facile synthesis of ultralong MnO_2 nanowires as high performance supercapacitor electrodes and photocatalysts with enhanced photocatalytic activities, CrystEngComm 16 (2014) 9999–10005.

[49] X. Chen, F. Zhang, Q. Wang, X. Han, X. Li, J. Liu, H. Lin, F. Qu, The synthesis of ZnO/SnO_2 porous nanofibers for dye adsorption and degradation, Dalton Trans. 44 (2015) 3034–3042.

[50] A. Mohammad, K. Kapoor, S.M. Mobin, Improved photocatalytic degradation of organic dyes by ZnO-nanoflowers, Chem. Select 1 (2016) 3483–3490.

[51] A. Bhattacharjee, M. Ahmaruzzaman, CuO nanostructures: facile synthesis and applications for enhanced photodegradation of organic compounds and reduction of p-nitrophenol from aqueous phase, RSC Adv. 6 (2016) 41348–41363.